Earth and Planetary Science Letters 492 (2018) 47–58

Contents lists available at ScienceDirect

Earth and Planetary Science Letters

www.elsevier.com/locate/epsl

Correlating the electrification of volcanic plumes with ashfall textures at Sakurajima Volcano, Japan

Cassandra M. Smith [a,*], Alexa R. Van Eaton [b], Sylvain Charbonnier [a], Stephen R. McNutt [a], Sonja A. Behnke [c], Ronald J. Thomas [d], Harald E. Edens [d], Glenn Thompson [a]

[a] University of South Florida, School of Geosciences, Tampa, FL, United States of America
[b] U.S. Geological Survey, Cascades Volcano Observatory, Vancouver, WA, United States of America
[c] Los Alamos National Laboratory, Los Alamos, NM, United States of America
[d] New Mexico Institute of Mining and Technology, Department of Physics, Socorro, NM, United States of America

ARTICLE INFO

Article history:
Received 7 September 2017
Received in revised form 26 March 2018
Accepted 27 March 2018
Available online 11 April 2018
Editor: T.A. Mather

Keywords:
Sakurajima Volcano
volcanic lightning
volcanic ash texture
vulcanian eruption
volcano monitoring

ABSTRACT

Volcanic lightning detection has become a useful resource for monitoring remote, under-instrumented volcanoes. Previous studies have shown that the behavior of volcanic plume electrification responds to changes in the eruptive processes and products. However, there has not yet been a study to quantify the links between ash textures and plume electrification during an actively monitored eruption. In this study, we examine a sequence of vulcanian eruptions from Sakurajima Volcano in Japan to compare ash textural properties (grain size, shape, componentry, and groundmass crystallinity) to plume electrification using a lightning mapping array and other monitoring data. We show that the presence of the continual radio frequency (CRF) signal is more likely to occur during eruptions that produce large seismic amplitudes (>7 μm) and glass-rich volcanic ash with more equant particle shapes. We show that CRF is generated during energetic, impulsive eruptions, where charge buildup is enhanced by secondary fragmentation (milling) as particles travel out of the conduit and into the gas-thrust region of the plume. We show that the CRF signal is influenced by a different electrification process than later volcanic lightning. By using volcanic CRF and lightning to better understand the eruptive event and its products these key observations will help the monitoring community better utilize volcanic electrification as a method for monitoring and understanding ongoing explosive eruptions.

1. Introduction

Volcanic lightning has the potential to inform about the physical processes taking place during explosive eruptions, especially at under-monitored volcanoes (Hoblitt, 1994; Bennett et al., 2010; McNutt and Williams, 2010; Cimarelli et al., 2016; Behnke and McNutt, 2014; Van Eaton et al., 2016). Although the operational use of volcanic lightning is in its infancy, a major goal is to determine relationships between electrical activity, eruptive intensity, and ash content, which are important factors for aviation hazards and downwind communities.

Volcanic plumes differ from thunderstorm clouds by the presence of volcanic tephra, their aerosol and gas contents, as well as temperature profiles and methods of convection. The addition of silicate particles adds to the types of charging that contribute to plume electrification. Thunderstorms develop charge primarily through collisional ice-graupel charging. The non-inductive charging of graupel (soft hail) is the most widely accepted theory (MacGorman and Rust, 1998). By comparison, the initially higher temperatures, seen in the near-vent portions of volcanic plumes, inhibit the development of graupel (Van Eaton et al., 2015). Therefore, ice charging mechanisms become important to plume lightning developing in the upper regions of volcanic plumes where sub-freezing temperatures may promote ice formation (Saunders et al., 2006; Williams and McNutt, 2005; Durant et al., 2008; Arason et al., 2011; Schill et al., 2015; Van Eaton et al., 2015, 2016). During initial plume formation, magma fragmentation (fracto-emission) and volcanic ash collisions (triboelectrification) are likely the dominant mechanisms of charging (James et al., 2000, 2008; Forward et al., 2009; Lacks and Sankaran, 2011; Houghton et al., 2013; Mendez-Harper et al., 2015; Mendez Harper and Dufek, 2016). The presence of near-vent plume electrification may hold insights into

* Corresponding author.
E-mail address: smithcm09@gmail.com (C.M. Smith).

https://doi.org/10.1016/j.epsl.2018.03.052
0012-821X/

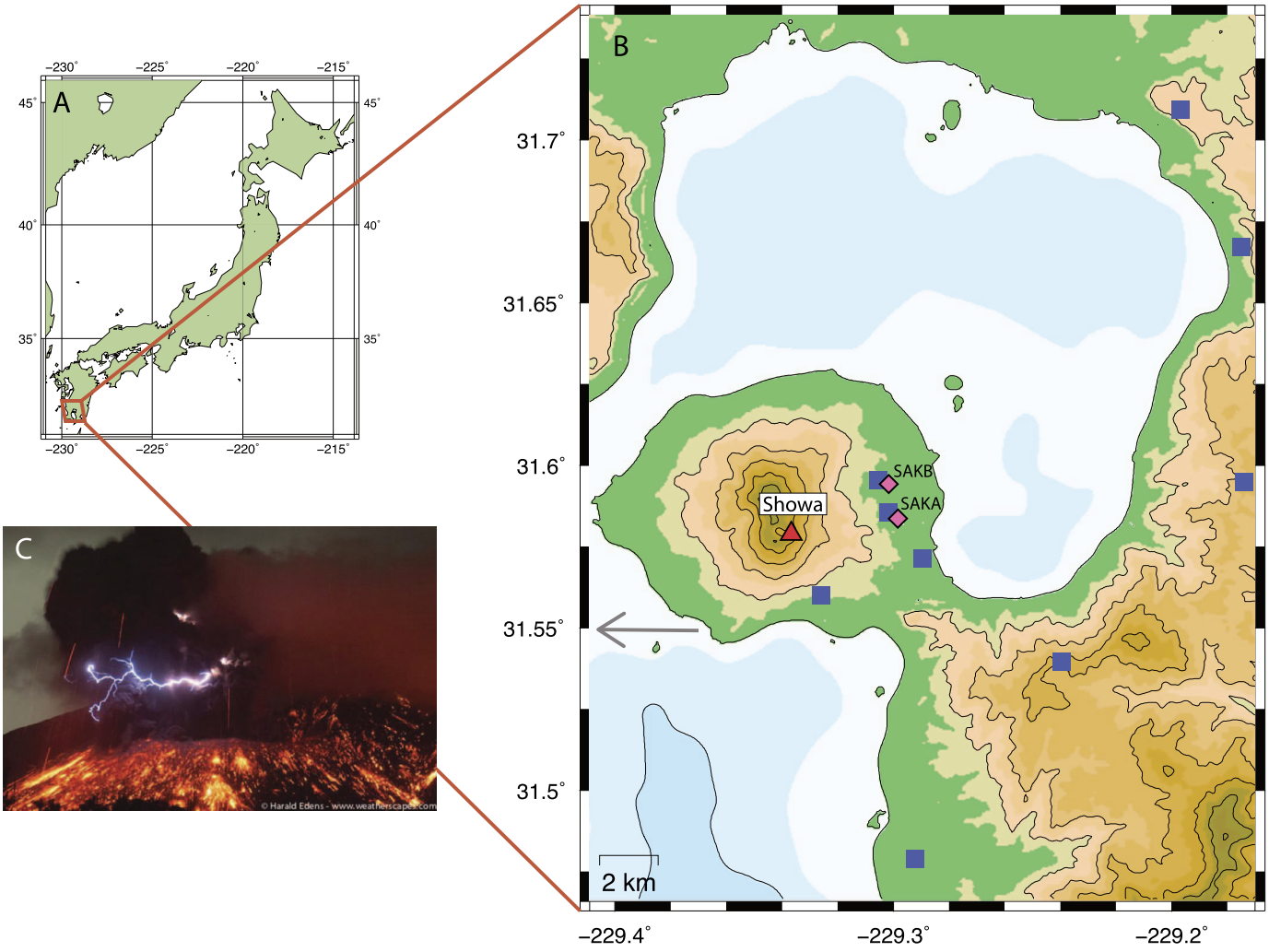

Fig. 1. (A) Index map of Japan, with study location boxed in red. (B) Map of Sakurajima Volcano instrument sites. The gray arrow points in the direction of Kagoshima ~8 km to the west, outside the frame of the map. The red triangle represents the location of Showa crater. The two pink diamonds represent seismic stations, SAKA and SAKB respectively. SAKA is located at the Kurokami lab site where the ash samples were collected. The nine blue squares represent the locations of the individual Lightning Mapping Array sensors. Panel C shows a photograph of volcanic lightning taken by co-author Harald Edens during the field campaign. (For interpretation of the colors in the figure(s), the reader is referred to the web version of this article.)

volcanic processes such as fragmentation efficiency and eruptive intensity (Cimarelli et al., 2014; Cashman and Scheu, 2015). There is no prior work in the area of linking ash textural parameters to quantified lightning metrics from an actively monitored eruption.

For this study, volcanic lightning was recorded at Sakurajima Volcano, Japan using the Lightning Mapping Array (LMA) from 29 May–5 June 2015. This follows previous studies of LMA-detected electrical activity at volcanoes such as Eyjafjallajökull (Behnke et al., 2014), Augustine (Thomas et al., 2007, 2010), and Redoubt (Behnke et al., 2013). From these previous investigations, it has become clear that volcanic eruptions produce a unique signal, known as *continual radio frequency* impulses (CRF), that is not present in regular thunderstorms. Our study focuses on determining relationships among: 1) the presence or magnitude of volcanic plume electrification in the form of CRF; 2) quantifiable ash characteristics; and 3) maximum seismic amplitudes for a set of monitored eruptions at Sakurajima during 2015. Correlations among these variables may allow one to use the properties/features of volcanic lightning to invert for the properties of the ejected ash and the eruptive intensity. This could help in the future monitoring of remote volcanoes.

2. Background

2.1. Sakurajima Volcano and ash analysis with respect to plume electrification

Sakurajima Volcano is located within the Aira Caldera in southern Kyushu Japan and is a <13,000 yr old edifice that grew 8 km south of the center of the Aira Caldera (Fig. 1) (Okuno et al., 1997). Historically, Sakurajima has erupted from multiple vents. The southern vents, Minami-dake and Showa are currently active (Okuno et al., 1997). For the past ~50 yr, Sakurajima has been consistently erupting with small (VEI 2) Vulcanian eruptions producing ash fall that reaches Kagoshima, approximately 8 km west (population ~600,000).

Vulcanian eruptions, such as those at Sakurajima, typically produce discrete explosions but may also be composed of a series of explosions that may continue for days or years (Clarke et al., 2015). The plumes of Vulcanian eruptions do not typically inject into the stratosphere and are thus lower risk for aviation. However, the study of these common, smaller plumes adds to an understanding of the smaller end-member of explosive volcanism and provides context for the analysis of rarer, large events. Sakurajima's eruptions range from pale, gas-rich puffs to dark, ash-rich jets, which

develop into the cauliflower shaped plumes characteristic of Vulcanian eruptions (Clarke et al., 2015). At Sakurajima these plumes rarely ascend more than 5 km into the atmosphere (Showa vent elevation ~750 m) with the majority of the plumes recorded for this study only reaching 0.5–3 km above the vent. A detailed analysis of how plume dynamics relate to the development of volcanic lightning will be examined in future work.

At Sakurajima, Miwa et al. (2009) studied the temporal relationship between ash textures and explosion quake characteristics to investigate conduit processes for a set of historic eruptions at Minamidake crater from 1974–1987. Miwa et al. (2009) looked at the componentry, groundmass crystallinity, and microlite number density (MND). They found positive correlations between MND and seismic amplitudes as well as between MND and decompression rates. One motivation of this paper is to further investigate this relationship by including more ash samples taken from a wider range of event sizes. This is important because linking ash textures with seismicity may shed light on processes of magma ascent, fragmentation, and eruptive intensity.

We note that the previous work by Miwa et al. (2009) examined ash from Minamidake crater while this study focuses on ash from Showa crater. Iguchi et al. (2013) showed that the two craters share a common magma chamber (~5 km depth). Two main deformation sources are interpreted as magma chambers, one main chamber at 10 km depth centered on Aira caldera and another at 5 km beneath Minamidake with a branched conduit off-shoot feeding Showa crater (Iguchi et al., 2013). Aramaki and Kobayashi (1986) showed that the chemistry of this magma source has remained consistent since 1955. Iguchi et al. (2013) showed the depth to explosion ranges from 0–2 km for Showa crater and from 2–4 km for Minamidaki. These differences in explosion depth, as well as potential differences in conduit shape may result in different ash properties, such as shape or componentry. However, the comparison between our study of MND and maximum seismic amplitude with Miwa et al.'s (2009) prior work on this relationship is still valuable to see if it is a universal or specific relationship.

Miura et al. (2002) investigated grain size distributions in Sakurajima plumes in relation to the potential gradient at the ground (using field-mill-type electrometers) as well as charge-mass ratios of falling ash (using a parallel plate apparatus). They inferred that finer ash had a net negative charge. Laboratory experiments have confirmed that particle size and span directly impacts charge segregation in granular systems (Miura et al., 2002; Forward et al., 2009; Lacks and Sankaran, 2011; Houghton et al., 2013; Mendez Harper and Dufek, 2016). Lacks and Sankaran (2011) found that within a sample the (relatively) smaller particles tend to become negatively charged during inter-particle collisions. This charging phenomenon has also been seen in other environments such as haboob dust storms (Williams et al., 2009). The 2010 Eyjafjallajokull eruption had a high level of recorded electrical activity; with peak flash rates reaching 1 flash per minute and 7700 discharges detected throughout the explosive period of the eruption (Bennett et al., 2010; Arason et al., 2011; Behnke et al., 2014). During this eruption Dellino et al. (2012) noted that the ash changed in shape from blocky to more angular, but the timing with respect to electrical activity was not investigated. In this study, the variation in ash shape will also be compared with electrical activity. If electrical charge is being generated from enhanced fracto-emission of ash particles during milling in the conduit this may be recorded in more equant particle shapes during times of high electrification.

2.2. Background on volcanic lightning

Lightning is common in Sakurajima's ash columns (Lane and Gilbert, 1992; James et al., 2008; Aizawa et al., 2010; Cimarelli et al., 2016; Aizawa et al., 2016). Lightning produces broadband electromagnetic radiation. High frequencies (i.e. VHF) are best detected at close range (hundreds of kms) and are used by the Lightning Mapping Array (LMA), which was developed by The New Mexico Institute of Mining and Technology (Rison et al., 1999; Hamlin, 2004; Thomas et al., 2004; Behnke and McNutt, 2014). This is the detection system utilized in the current study.

The LMA detects VHF radiation associated with the electrical breakdown of air as an impulse or "source" of VHF radiation (Behnke and McNutt, 2014). These sources can be located in 3-D space and grouped into distinct electrical discharges by type of event using the XLMA flash algorithm, which is based on timing and location of the sources (Thomas et al., 2003; Behnke et al., 2013).

There are three main divisions of volcanic lightning (McNutt and Thomas, 2015): (1) plume lightning occurs in the upper region of the plume, sometimes even after plume detachment. It is similar to lightning in ordinary thunderstorms and may reach flash lengths of greater than 10 km. Plume lightning occurs due to charge separation – facilitated by separation of particles with different settling speeds – in the upper, buoyant portions of the plume (Behnke and Bruning, 2015). (2) Near-vent lightning is of smaller length and typically occurs close to the vent during active jetting episodes, sometimes making ground contact with the edifice. It is characterized by its location in the gas-thrust portion of the plume and its visual proximity to the vent. (3) Continual radio frequency (CRF) impulses, are observed close to the vent (Thomas et al., 2010; Behnke et al., 2013, 2014; McNutt and Thomas, 2015). CRF is an ensemble of radiation sources, which occur over several seconds (Fig. 9a of Behnke et al., 2013), produced by a discharge with poorly known properties. The nomenclature for volcanic lightning studies is evolving. Previous literature has referred to CRF as "vent discharges" – in line with the thinking that this signal was caused by leader-forming electrical discharges on the order of 10–100 m in length. However, new research into the electrical properties of CRF (Behnke et al., 2018) shows that CRF is not produced by small leader-forming discharges but is rather a signal related to a different discharge process. CRF has been recorded specifically in conjunction with the high-velocity jet of the eruption column and has been seen only at volcanoes, with no analogue in thunderstorm lightning (Thomas et al., 2010). This makes CRF interesting because it may provide a means to distinguish between volcanic and meteorological lightning.

The two main parameters of electrical activity that will be discussed in this paper are the number of located sources (NLS) and the presence of continual radio frequency (CRF) impulses. The NLS is a count of all VHF sources that were located by the LMA for a given time and region of interest. The NLS represents all the electrical activity that was located for the eruptive event. The NLS does not distinguish between types of electrical activity such as lightning flashes or CRF, though the two are easily distinguishable by eye in the LMA data.

3. Methods

3.1. Ashfall sampling and preparation

From 29 May–5 June 2015, multiple explosive events per day occurred at Sakurajima's Showa Crater, from a minimum of 118 recorded seismic/infrasound events on 1 June to a maximum of 450 recorded seismic/infrasound events on 5 June. These events were recorded using a black and white low-light, video camera (Watec) as well as a thermal infrared camera (FLIR SC 660) from the Kurokami observation area 3 km east of the vent (Fig. 1). Plume heights of 500 m–3100 m above the vent were determined using a combination of our video estimates and the Japanese

Table 1
Ash collection times with corresponding plume onset times, seismic event onset times, and collected mass of ash. (All dates and times in UTC.)

SAK sample	Collection date	Collection time	Watec[c] plume event time	Corresponding seismic/ infrasound event time	Mass of sample (g)	Maximum seismic amplitude (um)	Number of located electrical sources (NLS)	CRF	Estimated plume height above vent (m)	Notes on source of plume height
1	5/29/15	9–9:15	8:12	8:12	0.24	8.5	6317	Yes	2900	JMA
3	5/29/15	9:15–10:15	9:33	9:33	0.6	0.5	46	No	1700	Watec estimation
5	5/30/15	10:05–10:21	NA	9:15, 9:30	1.74	60.1	105	Yes	NA	NA
7	5/30/15	6:30–10:00	NA	9:15, 9:30	10.84	60.1	105	Yes	NA	NA
10	5/31/15	8:29–8:48	NA	8:13	18.97	13.1	235	Yes	2950[a]	VAAC altitude recorded at 8:29
11	5/31/15	8:48–2:35	NA	11:09	15.21	31.8	22	Yes	NA	NA
19	6/4/15	7:00–7:10	6:22, 6:26, 6:37, 6:44, 6:49	6:22, 6:26, 6:37, 6:44, 6:49	0.77	1.8	18	No	700	FLIR estimation
20	6/4/15	7:25–7:40	7:07, 7:17, 7:27	7:07, 7:17, 7:27	1.97	1.6	81	No	2100	JMA
23	6/4/15	8:30–9:30	8:06, 8:23	8:06, 8:23	0.69	1.0	25	No	500	FLIR estimation
24	6/4/15	8:15–10:00	9:32, 9:52	9:32, 9:52	6.29	1.6	4	No	1800	JMA
25	6/4/15	10:00–10:45	10:34	10:34	0.45	11.1	1703	Yes	3100	JMA
26	6/4/15	10:45–11:45	10:34, 11:05	10:34, 11:05	0.31	7.1	1137	Yes	3100, 1100	JMA, Watec estimation
27	6/4/15	11:45–12:39	NA[b]	12:21	2.66	1.7	149	No	1800	JMA recorded at 12:04
28	6/4/15	12:39–13:39	NA[b]	12:41, 12:46	1.42	2.1	37	No	1800	JMA
30	6/5/15	6:25–6:30	6:04	6:04	60.79	2.3	50	No	1300	Watec estimation

[a] VAAC Values are given as altitude above sea-level. This value has been normalized to match the other values of elevation above vent.
[b] There is plume footage but the GPS clock was malfunctioning so only the hour is known.
[c] Watec is the low-light camera used for continual plume observations.

Meteorological Agency and Volcanic Ash Advisory Center reports (Table 1). Showa crater has an elevation of approximately 750 m above sea level.

Ashfall deposits were collected from clean, exposed surfaces at the Kurokami site approximately 3 km east of Showa crater (Fig. 1). Metal sheets were laid out during heavier ash fall to aid in temporal ash sampling (Table 1). For each sample, the duration and time of collection were recorded. The start time of the eruption producing each ash sample was not recorded while in the field. To correlate the ashfall samples to specific eruptions, the low-light video footage was examined for the time starting at the collection time and working backwards to determine the start time of events producing a plume that traveled over the Kurokami collection site (Table 1). Such visual data helped us confidently correlate ash samples with the correct plume and geophysical data. In the case of poor visibility due to weather (samples 5–11) the seismic and infrasound records were examined to determine the closest event that likely generated the ash.

The ash samples were weighed and subsampled for grain size, componentry, and SEM analyses. Material used for componentry and SEM imaging was manually sieved at >125 μm. The fines portion (<125 μm) was archived and the >125 μm portion was used for the rest of the preparation. This fraction was chosen because it is the lower limit for which optical componentry could be reasonably accomplished. Additionally, most samples were composed of less than 20 g of material, and we wished to retain as representative of a portion as possible for analysis. The >125 μm fraction was triple washed in distilled water, rinsed with ethyl alcohol, and dried to remove sulfate precipitates and adhering fines.

An important limitation of this study is the "representativeness" of the ash samples. We collected the samples from a single location, not from the entire area covered by each ashfall. Therefore, the data are not representative of the total particle population produced by each explosive event. However, the consistent collection location, generally downwind of the volcano, and relatively narrow range of eruption energies (plume heights 0.5–3 km) does allow a comparison across samples. Additionally, the Kurokami sample site is a common sample site for ash from Sakurajima, including ash collection systems run by the local observatory. Therefore, although not as representative as a total grain size distribution, our sample set represents a good starting point for this type of analysis.

Another limitation is linking the ash sample to a known eruptive event. Field conditions necessitated some assumptions when determining the originating plume using video and seismic data streams. Therefore, the explosive events without visual confirmation (ashfall samples 5–11), have an increased possibility of the sample being assigned to an incorrect seismic event.

3.2. Particle size distributions and morphology

Grain size distributions of each ashfall sample were determined using a Beckman Coulter LS 13 320 SW Laser Diffraction Particle Size Analyzer (LDPSA) at the U.S. Geological Survey Cascades Volcano Observatory in Vancouver, WA. The instrument measures the scattering of light from a 780 nm laser passing through water-suspended particles to determine their grain size distribution from 0.4 μm to 2 mm (in terms of vol.%). We assumed a refractive index of 1.55 and absorption coefficient of 0.001 consistent with volcanic glass of intermediate composition (Horwell, 2007).

The resulting distribution curves are described by the summarizing statistics of the mean (μm and Φ), the sorting deviation (σ_1), and the standard deviation (μm), where the Φ value is defined as the negative log of base two of the particle diameter in mm. The more positive the Φ value the smaller the particle. The equations

Table 2
Ashfall componentry, size, and shape results.

SAK sample	Total number of grains picked	Glass (%)	Lithic (%)	Crystal (%)	% of glass grains that are not 'fresh'	Total number of grains[a]	Mean aspect ratio[a]	Standard deviation of aspect ratio[a]	Skew of aspect ratio[a]	Mean diameter (μm)[b]	Standard deviation of mean diameter[b]	Folk and ward mean diameter (phi)[b]	Folk and ward sorting (phi)[b]
1	141	64.5	7.8	27.7	6.6	3544	0.65	0.20	−0.63	64.73	16.13	3.9	0.38
3	240	57.5	8.8	33.8	5.8	13805	0.64	0.21	−0.61	113.20	91.70	3.1	1.01
5	221	73.3	2.7	24.0	9.3	21505	0.68	0.20	−0.67	238.10	159.00	2.1	1.53
7	252	77.8	5.2	17.1	10.2	7059	0.61	0.23	−0.59	411.30	333.40	1.3	1.8
10	225	64.0	1.8	34.2	6.9	29820	0.67	0.21	−0.72	185.20	119.80	2.4	1.53
11	201	69.7	4.0	26.4	10.7	116356	0.69	0.18	−0.64	117.30	105.70	3.1	1.83
19	254	62.2	4.7	33.1	12.7	6506	0.46	0.25	0.18	162.90	47.85	2.6	0.42
20	272	61.4	10.7	27.9	9.0	4227	0.48	0.25	0.10	129.60	44.72	2.9	0.48
23	200	63.0	11.5	25.5	6.3	4805	0.53	0.26	−0.18	111.10	43.37	3.2	0.58
24	242	57.4	16.5	26.0	17.3	24536	0.67	0.20	−0.74	80.99	41.36	3.6	0.99
25	149	62.4	8.7	28.9	11.8	6419	0.60	0.25	−0.58	89.79	47.80	3.5	0.61
26	245	60.4	8.6	31.0	6.8	10306	0.50	0.27	0.05	120.90	65.81	3.0	0.74
27	235	60.0	2.1	37.9	4.3	15438	0.68	0.19	−0.72	103.50	36.83	3.3	0.83
28	275	60.4	2.9	36.7	6.0	20235	0.68	0.20	−0.67	69.63	45.26	3.8	0.85
30	255	60.0	8.2	31.8	15.0	97497	0.67	0.19	−0.69	131.00	138.90	2.9	1.91

[a] Results are from the Malvern PharmaVision and are reported as numeric distributions.
[b] Results are from the Laser Diffractor and are reported as a volume distribution. Columns 2–6 are the results of componentry analysis.

for the mean and deviation statistics in Φ are from Folk and Ward (1957) and calculated by the LDPSA.

Particle shape characteristics were analyzed using the Malvern PharmaVision 830 (MPV830) at the University of South Florida. The MPV830 uses static 2-D images of the ash, evenly dispersed over a glass plate, to calculate parameters such as diameter and roundness of individual grains (reported as a numeric distribution). The MPV830 uses a camera attached to a microscope and computer to scan, photograph, and analyze the particles. For this analysis, a 20× lens was used in combination with 4× and 0.5× magnification lenses in order to fully analyze a range of particle sizes from 0.3 μm to 2 mm. A 20 mm × 30 mm area of the glass plate was analyzed for each sample (except for sample 7 where it was 20 mm × 20 mm) resulting in 3500 to 120,000 grains being measured per sample (Table 2). The diameter calculated within the MPV830 software is the circle equivalent diameter (Leibrandt and Le Pennec, 2015). The 2-D roundness ratio is similar to the aspect ratio defined by Leibrandt and Le Pennec (2015), it is calculated within the MPV830 software by comparing the length and width of the grain; a perfect circle has a roundness of 1.0 while a rod shaped particle would have a roundness close to 0. However, throughout this paper we will use the term aspect ratio when discussing this roundness parameter. This is to help clarify that we are discussing the shape of the particle (elongate or equant) and not how angular or smooth the edges are. A benefit of this instrument is that it can assess many thousands of grains per single analysis. However, the entire ashfall sample is analyzed, not just the juvenile material (which is the component of interest when investigating magma fragmentation). The camera used by the MPV records backlit black and white 2-D images of the projected shape of each grain. It is not possible to use these images to discern the componentry of the grain.

3.3. Componentry

For each ashfall sample, between 140–275 ash particles were randomly selected from the >125 μm fraction and categorized for a componentry analysis using an optical microscope under reflected light at 40× magnification (Table 2). The categories selected for this study are juvenile glass, crystals, and altered/lithic grains (Fig. 2). Juvenile glass is defined by the high gloss sheen on black to dark brown particles. It is subdivided into fresh and non-fresh glass with the latter showing some minor pitting or abrasion. The fresh particles were more numerous than the non-fresh and featured smooth sides with clearly defined edges and no pitting (Table 2). The glass particles are mainly composed of dense, bubble-free glass, with microlites visible under SEM, with the rare vesicle. The crystal fraction consists of free crystals (mostly plagioclase and pyroxenes) with a small amount of adhering glass ($\lesssim$10%). The altered/lithics category consists of any particle showing clear signs of alteration, including highly pitted and abraded edges/faces, and/or reddish oxidation, as well as particles of non-volcanic bedrock. A standard deviation from repeated measurements determined error bounds on the componentry measurements to be less than ±3%.

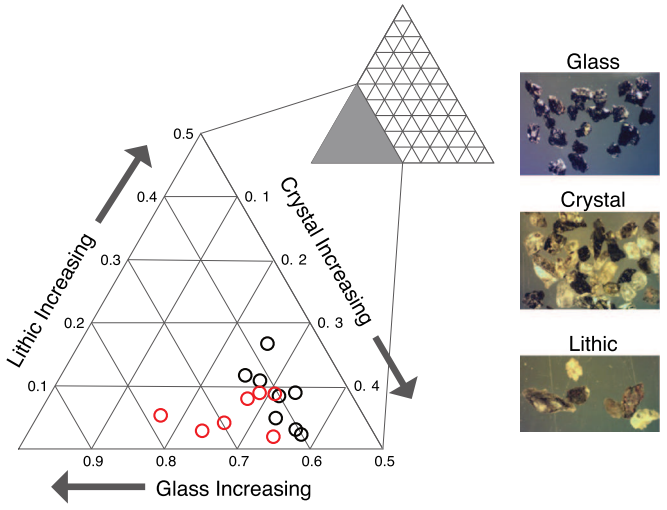

Fig. 2. Componentry ternary diagram. Red circles are events that had continual radio frequency (CRF) impulses. Black circles are events without CRF. The inset microphotographs show examples of the componentry divisions. The glass particles are glossy and black to dark brown with smooth sides. The crystal particles are free crystals with smooth and distinct crystal faces and ranged from clear to black. The lithic particles group included any particle showing clear signs of alteration or particles of non-volcanic bedrock.

3.4. Microlite number density and crystallinity

The plagioclase microlite number density (MND) has been related to the average decompression and ascent rates of the magma as it moves up the conduit (e.g. Toramaru et al., 2008). Plagioclase was chosen for the MND analysis to facilitate comparisons

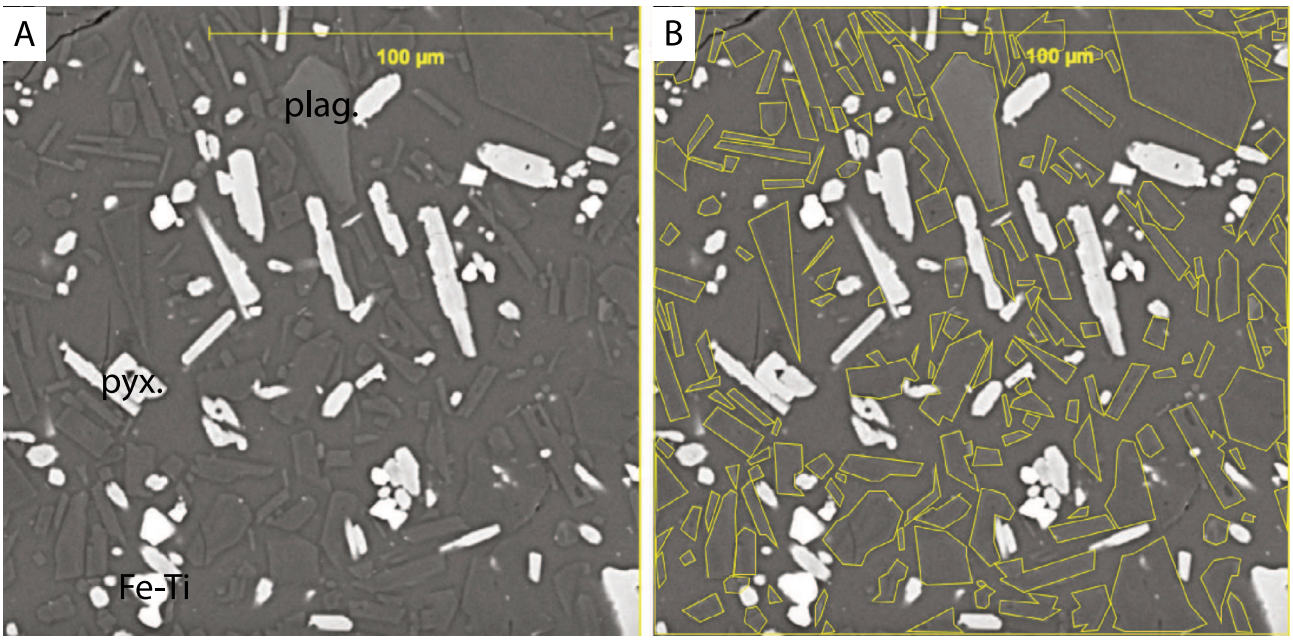

Fig. 3. Scanning electron microscope image of part of a fresh glass ash particle. (A) Raw image with microlites of plagioclase, pyroxenes, and Fe–Ti oxides labeled, (B) yellow outlines indicate plagioclase microlites analyzed for microlite number density calculation.

with previous work at Sakurajima (Miwa et al., 2009) using the method of Toramaru et al., 2008. An increase in MND is related to a faster decompression rate (Toramaru et al., 2008). Additionally, higher MND values have been related to larger amplitude (more explosive) seismic events at Sakurajima (Miwa et al., 2009).

From the fresh glass portion of the componentry analyses, approximately 20 grains were randomly picked for SEM mounting and analysis. The particles were mounted following the method of Lowe (2015). Grain mounts were carbon coated and imaged using an Aspex EXPress desktop SEM at the Cascades Volcano Observatory of the U.S. Geological Survey. A working distance of 15–17 mm and beam energy of 20 kV were used under vacuum to obtain images of exposed grain surfaces. SEM imaging of these grains revealed microlites of plagioclase, pyroxenes, and Fe–Ti oxides.

To determine the plagioclase MND of the ash particles, the SEM images were imported into ImageJ open source software (Schneider et al., 2012). The gray tone coloration between the plagioclase microlites and surrounding glass was too similar to allow for automatic thresholding. Therefore, each plagioclase crystal was manually identified and outlined (Fig. 3). ImageJ computed the total number of outlined microlites, and their 2-D geometrical characteristics. Between 7–10 grains were manually analyzed from each ashfall sample. The cross-sectional area of the grain visible in the SEM image was also calculated. The areal MND was calculated by taking the number of microlites in a specific ash grain divided by the area of the particle in µm. Miwa et al. (2009) used the grain size fraction from 350–500 µm. We did not have enough grains in the 350–500 µm fraction to perform a quantitative analysis that was representative of the total ash sample so we used the $>$125 µm fraction.

The plagioclase crystallinity was determined by taking the sum of plagioclase microlites areas divided by the total area of the grain (also referred to as the areal fraction of plagioclase) (Miwa et al., 2009).

3.5. Detecting electrical activity with the Lightning Mapping Array (LMA)

The LMA detects VHF (30–300 MHz) electromagnetic ration in a 6 MHz passband. This radiation is produced during the electrical breakdown of air, which occurs as conductive channels form (Rison et al., 1999). Impulsive radiation is recorded as numerous VHF 'sources' that, when correlated across several LMA stations, can be located to provide a three-dimensional map of the lightning discharge (Thomas et al., 2004). Lightning discharges are composed of a number of these 'sources'. Therefore, one useful statistic derived from the LMA data is the number of located sources (NLS). The larger the NLS, the more electrical activity was present in the plume. Electrical noise that would be recorded on the LMA is typically locally generated near the station and would therefore not be recorded on the multiple sensors needed to locate the source. Such noise may manifest in the located data due to chance correlations during data processing. These sources are differentiated from CRF in that noise is generally poorly located over diffuse areas whereas CRF is a well located group of sources located in the small region over the volcano and only occurs when the volcano is erupting. The influence of noise in our data has been significantly reduced by only using located sources that had a reduced chi-squared of 1 or less.

The LMA data for this study were collected from a 9-instrument network. The instruments were located on the eastern side of Sakurajima at a variety of azimuths and distances from the vent (Fig. 1). For this experiment the LMA passband was 66–72 MHz. The LMA data are processed from raw data to located sources using a time-of-arrival algorithm (Thomas et al., 2003). The NLS was determined by counting all of the located electrical sources within a 1 km $\times$ 1 km $\times$ 2 km (X $\times$ Y $\times$ Z) box around Showa Crater at Sakurajima.

Another observation drawn from the LMA is the presence of CRF. CRF occurs over relatively long durations (typically several seconds, but there is no defined upper limit), in contrast to the burst of radiation associated with a discrete lightning flash, which typically occurs over timescales of less than one second. In the LMA data we see CRF immediately, as soon as ash venting starts, even before the plume rises above the rim of the crater and into view. The onset of CRF is clear and is correlated with other geophysical signals, such as infrasound (Behnke et al., 2013; Behnke and McNutt, 2014). In this study, we characterize events using the presence of CRF, its duration (s), and its peak rate of occurrence (per 100 µs window). The peak rate of CRF was deter-

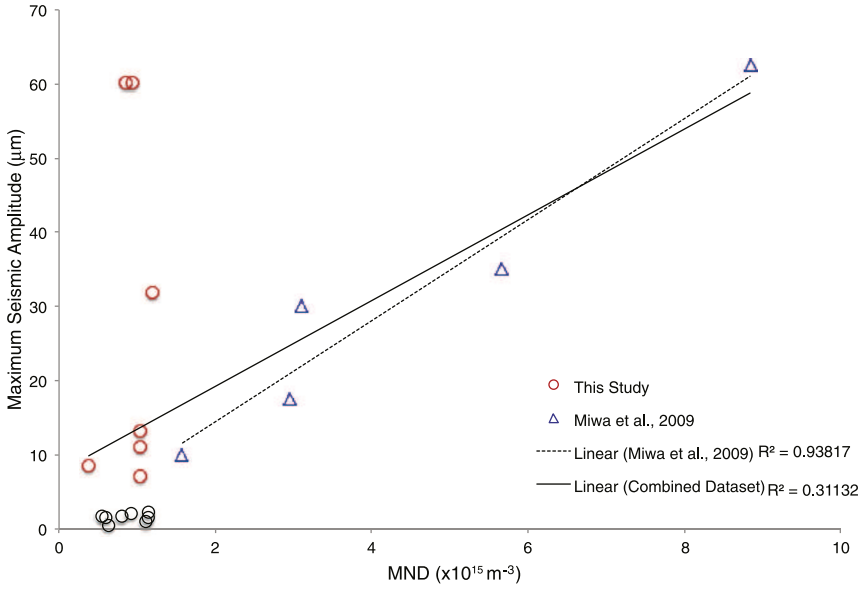

Fig. 4. Microlite number density (MND) and seismic comparisons. Compilation of data from this study (circles) and Miwa et al. (2009) (triangles) showing the relationship between MND and maximum seismic amplitude. Red circles are events that had continual radio frequency (CRF) impulses, black circles are samples that did not have CRF. There is a separation between events with and without CRF in relation to the maximum seismic amplitude. The original Miwa et al. (2009) data show a positive correlation between MND and maximum seismic amplitude. The addition of this study's data adds variance to this relationship in the lower portion of the MND scale.

mined from the unprocessed LMA data recorded by a single station. First, the raw source rate was smoothed to remove high-rate spikes caused by small lightning discharges. Then, the source rate was scaled by a normalization factor that takes into account the effective 'duty cycle' of the LMA station. The NLS and CRF are used here to investigate if relationships exist between volcanic electrification and measurable ash parameters.

3.6. Seismic measurements

The seismic data were recorded at 100 samples per second with a 2-station network located on the eastern side of Sakurajima. The instruments used were Nanometrics Trillium Compact 120 s Posthole 3-component broadband seismometers. During field deployment, the data were stored on a Nanometrics Centaur Digitizer. The reported seismic amplitude measurements are calibrated displacement values. These amplitudes are the absolute value of the maximum zero-to-peak amplitude recorded within an event on the vertical seismic channel. For those ash samples that represent multiple plume and seismic events (Table 1), we have used an average maximum seismic amplitude (µm). Because we had only two seismometers with a small azimuthal range ($<45°$), we were not able to account for any seismic radiation patterns that may have affected the seismic data.

4. Results and discussion

4.1. Componentry

The componentry results are shown in a ternary diagram in Fig. 2. The ashfall samples cluster in the glass-rich, lithic-poor section of the diagram with glass comprising 57–78%, lithics 2–17%, and crystals 17–38%. These percentages are determined from the number of particles of each category divided by the total number of particles analyzed for componentry in that sample. A pattern emerges when the data are color-coded for the presence of CRF. The majority of CRF-producing events have $<10\%$ altered or lithic grains and $>60\%$ glass. This may be indicative of the type of material involved in the electrification mechanism that produces CRF at Sakurajima: low lithic and high glass proportions point to events composed mainly of fresh, juvenile magma fragmenting to form glassy ash rather than the destruction of older, pre-existing lithic material in the vent or the solidified magma that caps the conduit between explosive periods.

4.2. Microlite number density (MND) and seismic data

Previous work by Miwa et al. (2009) found a positive correlation between the MND and the maximum seismic amplitude of explosion earthquakes at Sakurajima. The implication is that more eruptive energy (proportional to a higher seismic amplitude) is required to destroy a more established degassed magma cap (with greater microlite content). Although there are no electrical observations for the eruptions of Miwa et al. (2009), the comparison with our data is interesting because it sheds light on how ash characteristics may fit into other monitoring data-sets. We explore the relationship between MND and maximum seismic amplitude for ashfall from Sakurajima's Showa Crater, and compare with the Minamidake crater samples of Miwa et al. (2009). The MND values used by Miwa et al. (2009) were based on 5 large and well-characterized ashfall events from eruptions that took place between 1974–1982. Each average MND value was calculated from 4–5 individual particle MNDs. Our study looks at 15 samples over a narrower time range and somewhat smaller eruptions based on seismic amplitudes. The seismic station used to determine seismic amplitude in the Miwa et al. (2009) study was located at a different azimuth ($\sim 135°$ counter-clockwise from the station used in this study) but at a similar distance (2.7 km vs. 3 km) from the active crater. Therefore, we infer that the seismic data are comparable.

Combining the data of our study and Miwa et al. (2009) (Fig. 4) reveals some interesting observations. First, our data alone do not show a relationship between microlite number density and seismic amplitude ($R^2 = 0.02$), which contrasts to the strong relationship observed in the Miwa et al. dataset ($R^2 = 0.94$). It is worth noting that the outliers in the upper left of Fig. 4 represent two events during poor weather/visibility, meaning that the ashfall samples were correlated to the seismic amplitude based on only the time of collection, without the added video data to corroborate (adding some uncertainty). Second, the combined data sets do still support

Table 3
Microlite number density values and calculated average ascent velocities and decompression rates.

SAK sample	Number of samples	Mean microlite number density (MND) (m^{-3})	MND standard deviation (m^{-3})	Mean areal fraction of plagioclase	Areal fraction of plagioclase standard deviation	Average ascent velocity (m/s)	Decompression rate (Pa/s)
1	10	3.8×10^{14}	2.7×10^{14}	0.34	0.07	0.045	1107
3	10	6.4×10^{14}	4.3×10^{14}	0.35	0.12	0.064	1565
5	10	8.6×10^{14}	4.6×10^{14}	0.32	0.08	0.078	1912
7	10	9.6×10^{14}	5.0×10^{14}	0.30	0.05	0.084	2048
10	7	1.1×10^{15}	1.1×10^{15}	0.23	0.12	0.089	2183
11	10	1.2×10^{15}	6.7×10^{14}	0.25	0.06	0.097	2389
19	7	5.5×10^{14}	4.3×10^{14}	0.34	0.09	0.058	1420
20	10	1.1×10^{15}	6.0×10^{14}	0.27	0.04	0.094	2305
23	8	1.1×10^{15}	9.1×10^{14}	0.26	0.09	0.093	2271
24	10	6.0×10^{14}	3.3×10^{14}	0.31	0.08	0.061	1499
25	9	1.0×10^{15}	8.5×10^{14}	0.32	0.06	0.089	2176
26	10	1.1×10^{15}	4.7×10^{14}	0.29	0.09	0.089	2185
27	10	8.0×10^{14}	3.1×10^{14}	0.29	0.06	0.074	1826
28	10	9.3×10^{14}	4.7×10^{14}	0.28	0.06	0.082	2006
30	10	1.1×10^{15}	7.7×10^{14}	0.33	0.10	0.094	2309

a weak, positive correlation ($R^2 = 0.3$). Overall, our measurements introduce scatter into the original relationship proposed by Miwa et al. (2009), suggesting either a weaker correlation or a different mechanism for the smaller end of the scale of Vulcanian eruptions from Showa Crater.

Using the decompression rate to calculate average magma ascent rates, Miwa et al. (2009) shows that the Vulcanian eruptions they studied at Sakurajima had ascent rates of 0.11–0.35 m/s. The magma ascent rates determined in our study range from 0.04–0.09 m/s (Table 3). These values fall in between those given for effusive and Vulcanian eruptions in Miwa et al. (2009), indicating that the eruptions studied in this paper were smaller Vulcanian events than those investigated by Miwa et al. (2009). Further investigations into this relationship at Sakurajima, as well as at other volcanoes, will help clarify the relationship between MND and maximum seismic amplitude.

By combining our data on the crystallinity (areal fraction of plagioclase) of the ash samples compared to the maximum seismic amplitude to that done by Miwa et al. (2009), we can see that the previous lack of correlation is maintained (Fig. S.1).

4.3. Seismicity and continual radio frequency (CRF) impulses

Fig. 5 shows a clear distinction between the seismic signals of events that produce CRF and those that do not (Fig. 5A). The events without CRF have longer seismic waveform durations (Fig. 5B and 5C). This may indicate that CRF is not present in events of steady ash and gas venting. The seismic events that correspond to detected CRF are shorter in duration indicating a discrete explosive pulse, associated with events of larger maximum seismic amplitude. The lowest seismic amplitude with CRF is 7.06 μm while the highest seismic amplitude without CRF is 2.32 μm. This clustering is even clearer when examining the maximum seismic amplitude individually (Fig. 5A). The increased seismic amplitude can be interpreted as an explosivity threshold required for generating CRF. Seismic amplitude is proportional to seismic energy so this amplitude threshold may indicate a minimum energy input required to initially fragment and/or accelerate the ash particles in the conduit, building up electrical charge that is detected as CRF. This overall observation does not extend to our estimated magma ascent rates, (S.2) – we see no relationship between the average magma rate (from microlites) and the magnitude of electrification or presence of CRF in the plume (Fig. S.2). One possibility is that the uncertainty of the ascent rate calculations is simply too great to expect any meaningful correlation. Alternatively, it is possible that the CRF charging mechanism is related to the energy of the final explosion rather than the time-averaged rate of magma ascent. Thus, the CRF occurs on shorter spatial and temporal scales than would be reflected in microlite growth. This shows that the explosion energy, as indicated by seismic amplitude, may not be well correlated with average magma ascent rate from microlites.

4.4. Grain size distributions

Fig. 6A shows the mean grain size following methods in Folk and Ward (1957) and sorting of the ashfall samples in Φ (phi) values. In general, the finer grained samples in our data-set are slightly better sorted ($R^2 = 0.3$). Fig. 6B shows a similar relationship of the mean grain size (as the 50th percentile) versus the standard deviation in microns. In other words, the finer-grained samples have a smaller standard deviation, indicating a narrower peak in the distribution.

There is no correlation between the ashfall grain size statistics and the production of electrical activity (in terms of CRF or NLS; Fig. 6). This lack of correlation holds even when we used the same grain size metrics proposed by Houghton et al. (2013) in their laboratory experiments on electrical charging (normalized span and modality; Fig. S.3). This is a surprising result given experimental work that has previously linked fine ash content (50–500 μm), which is a similar range to our samples, to enhanced electrical activity (Miura et al., 2002; Cimarelli et al., 2014; Forward et al., 2009; James et al., 2000; Mendez-Harper et al., 2015). A future study with more samples that are representative of the total grain size distribution may result in findings more in line with the experimental results.

4.5. Particle shape

We investigated relationships between the plume electrification and the mean aspect ratio of ash particles as calculated from the MPV830 optical imager. We also looked at the skew of these shape distributions. For lower mean aspect ratio (more elongate particles), there is a slight positive skew to the distribution, but as the mean aspect ratio increases (more equant particles) the distributions become more negatively skewed (Fig. 7A, $R^2 = 0.94$). This indicates that ashfall with more equant grains overall also contains a small amount of elongated material (Fig. 7D). We note that CRF-producing eruptions are more likely to produce equant grains (high aspect ratios). Fig. 7A shows that all but one of the CRF-producing eruptions cluster in the lower right-hand portion of the plot – these are the ashfall samples with more equant grains over-

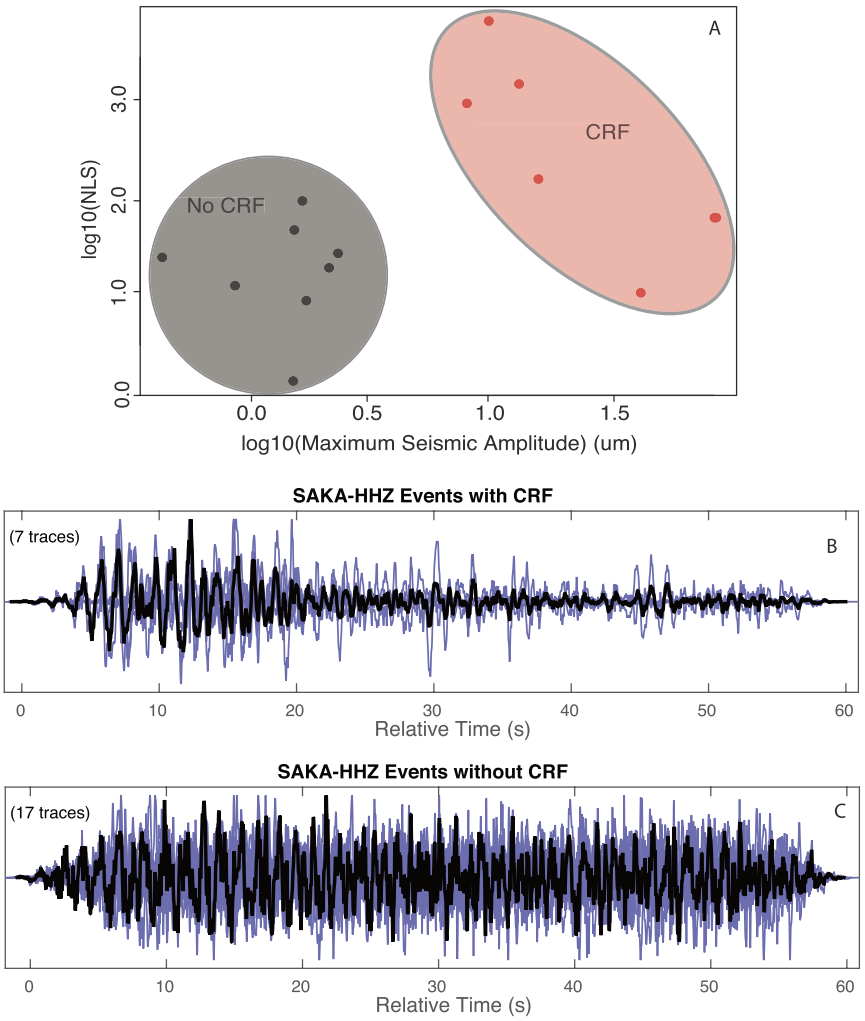

Fig. 5. Plots of the number of located sources (NLS) and seismic amplitude. (A) Plot of the $\log_{10}$ of the NLS against the $\log_{10}$ of the maximum seismic amplitude. Red circles (enclosed by the large red oval) are events that had continual radio frequency (CRF) impulses, black circles (enclosed by the large grey circle) are events that did not have CRF; (B) Stack of vertical seismic traces for events with CRF; (C) Stack vertical seismic traces for events without CRF. Both stacks have normalized amplitudes as the y-axis.

all and a small amount of elongate particles (as a long tail in the shape distribution, Fig. 7D).

One possible explanation is that the more equant particle shapes are due to milling in the conduit (secondary fragmentation). The milling process has transformed the elongate grains into more equant ones, leaving behind a tail of elongate particles in the shape distribution, as seen in Fig. 7D. After primary fragmentation of the rising magma, it travels up the conduit toward the atmosphere. Particles in this high-energy, high-concentration flow undergo vigorous collisions with other particles and the side of the conduit. The laboratory experiments of Dufek et al. (2012) showed that increased fragmentation depth in combination with larger pumice clasts (>1 cm) resulted in the most effective fragmentation, with no disruptive collisions occurring for clasts <1 cm. Jones et al. (2016) investigated the fragmentation of andesite pumice blocks through rapid decompression, impact, and milling. They found that fragmentation through rapid decompression resulted in a large range of aspect ratios. However, fragmentation through milling gave the 250–500 μm ash a higher aspect ratio (more equant particles) and smaller range. A similar pattern is shown in Fig. 7D, which shows a sample where CRF was recorded in the explosive event, and where the ash particles are more equant. We also point out that there is no correlation between mean aspect ratio and particle diameter (Fig. S.4), so the link is with grain shape rather than size.

From these observations, we infer that the Sakurajima ash was created from a combination of initial fragmentation as well as the byproduct of the disruptive collisions of larger clasts traveling through the conduit. We can interpret CRF as being related to enhanced milling of particles in the conduit or initial gas thrust region. This hypothesis is supported by a parallel study done by Behnke et al. (2018) that shows that CRF begins prior to the plume rising to visible levels above the crater rim, indicating that it must originate within the shallow conduit or crater, where particle collisions and milling is facilitated by conduit constrictions as well as the high concentration of the gas-particle flow, which has not yet entrained large amounts of air (Jones and Russell, 2017). This indicates that, although CRF frequently occurred in samples with high aspect ratios and longer tails of elongate material, that these shape parameters likely do not affect the continued generation or separation of charge as the plume develops and becomes buoyant. Fig. S.5 shows that there is no significant relationship between the mean aspect ratio and the total NLS. This suggests that only the CRF signal is influenced by grain shape (related to milling in the conduit). We infer that other electrification processes, such as charge separation in turbulent eddies, become more important as the plume develops.

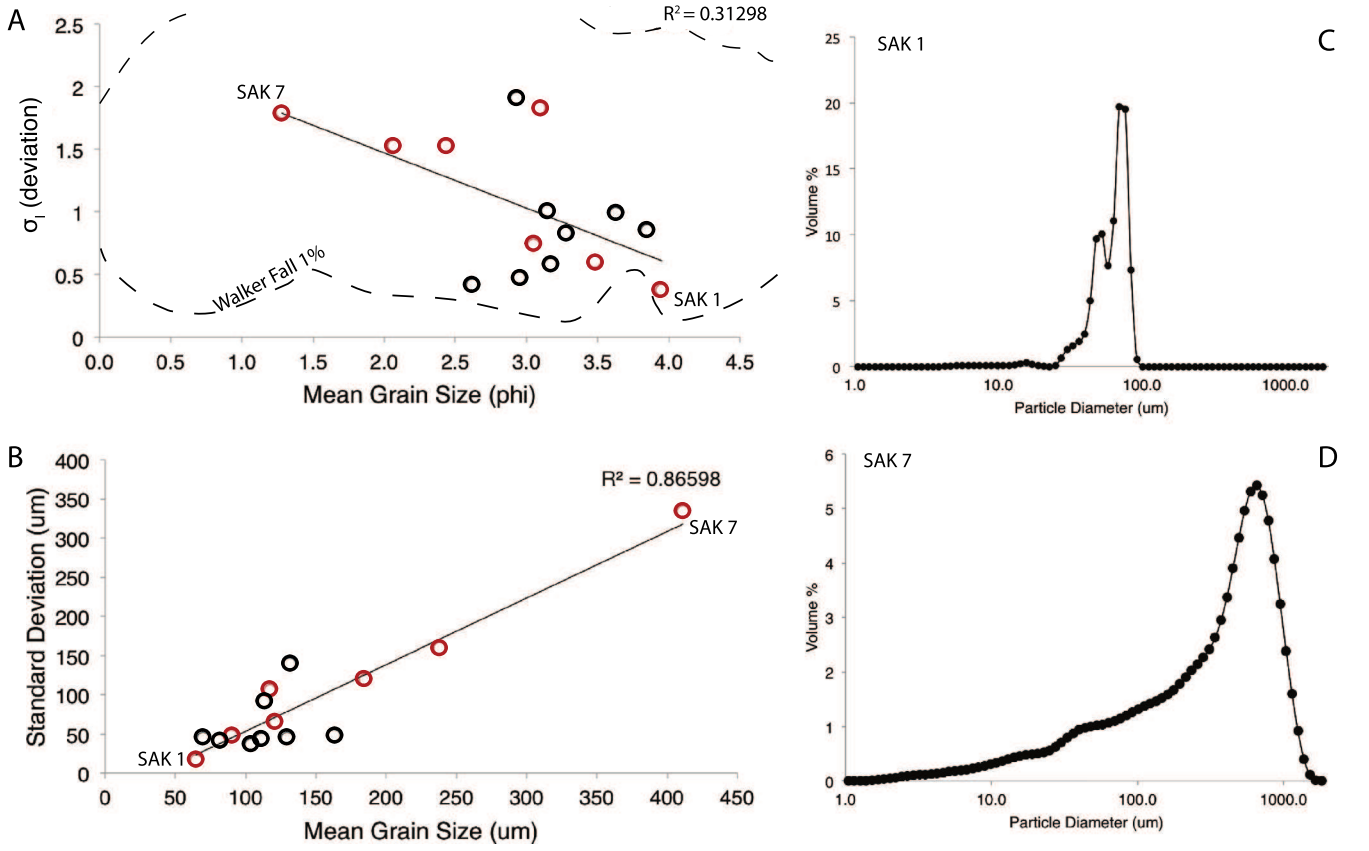

Fig. 6. Grain Size Distribution Statistics. (A) Folk and Ward's statistics of Deviation vs. Mean Diameter in Φ units; (B) Standard Statistical plot of Standard Deviation vs. Mean diameter in μm; (C) An example grain size distribution for sample SAK 1, showing low deviation, low standard deviation, and small grain size; (D) An example grain size distribution for sample SAK 7 showing high deviation, high standard deviation, and larger mean grain size. Lines in A and B are linear regressions. For all plots, red circles are events that have CRF.

4.6. CRF rate and duration

Finally, CRF was quantified by its peak rate of occurrence (per 100 μs window) and total duration (s). When compared to dataset of seismic and ash textural parameters we found no significant relationships (Fig. S.6A, B). Further study between quantified CRF with ashfall textures and geophysical signals from a variety of volcanic systems may help determine if the rate or duration of CRF hold useful insight into volcanic processes.

5. Conclusions

This study has examined the eruptive activity of Sakurajima Volcano in Japan with the overall goal of understanding the relationship between volcanic lightning and eruptive behavior. Fifteen ashfall samples were analyzed for grain size, shape, microlite number density, and componentry and compared to seismic signals and LMA measurements of plume electrification. The electrical properties of the plume are described by the total number of electrical sources and by the presence or absence of continual radio frequency impulses, an electrical signal that is unique to eruptions. By better understanding the charge generation behind CRF we hope to become better equipped to utilize measurements of plume electrification for active volcanic monitoring.

An important finding of this study is that CRF-producing eruptions at Sakurajima have unique characteristics based on (1) volcanic ash texture (componentry and particle shape) and (2) eruption dynamics (seismic amplitude and waveform shape). The key observations are summarized as follows:

- CRF occurs during eruptive events that are glassy and lithic-poor (>60% glass and <10% lithics). This indicates that CRF occurs more frequently when the eruption consists of fresh, actively fragmenting magma rather than recycled material.
- CRF is associated with volcanic ash rich in equant grains. We infer that the electrical charging is enhanced by milling in the conduit (secondary fragmentation) during ascent of the erupting mixture. The charging process likely occurs due to a combination of sources including initial and secondary fragmentation (fracto-emission charging) as well as non-destructive ash contact (triboelectric charging) in the high-velocity, high concentration region of the particle-laden flow.
- We have established an explosivity threshold required for generating CRF in small-scale eruptions. The electrical signal occurs in events defined by higher seismic amplitudes and shorter seismic durations. This suggests that CRF requires a high-energy, impulsive explosion to sufficiently fragment and accelerate the ash particles.
- The generation of CRF, but not total plume electrification, is relatable to grain shape. This suggests that milling in the conduit (resulting in more equant particles) influences the production of CRF, but that later in plume development other electrification processes become more important for the generation of volcanic lighting flashes.

Taken together these observations point towards CRF occurring in explosive events composed of freshly fragmented magma that undergoes milling in the conduit/early plume.

In this study, we were also able to examine the relationship between the maximum seismic amplitude of explosive eruptions at Sakurajima and the microlite number density of ash particles

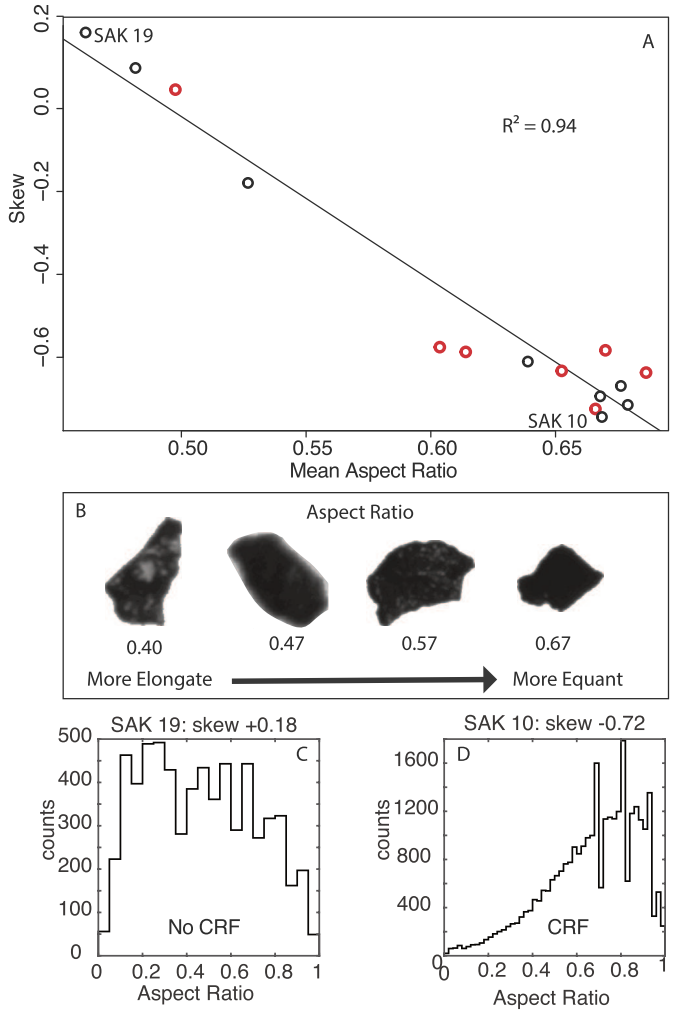

Fig. 7. Plots comparing particle aspect ratio with the skew of the aspect ratio's distribution. A) The skew of the distribution against the mean aspect ratio; B) The silhouettes are images from the MVP830 to show a range of particle aspect ratio; C) An example aspect ratio distribution showing sample SAK 19 with a skew of 0.18; D) An example aspect ratio distribution showing sample SAK 10 with a skew of −0.72; lines are linear regressions. For all plots, red circles are events that had continual radio frequency (CRF) impulses.

(a proxy for magma ascent rate). By including a suite of smaller-scale eruptions to the dataset of Miwa et al. (2009), we show that there is a larger range of variance associated with the relationship than previously documented. Future work clarifying the relationship between the magma ascent rate and eruptive seismicity will constrain the physical processes inside the conduit and how these may relate to other near-vent signals such as the production of CRF. We find that CRF is clearly associated with stronger, more impulsive seismic signals, but not to faster "overall" magma ascent rates determined from microlites. This suggests that CRF production is more sensitive to the final stage of magma fragmentation than to the time-averaged rate of ascent from depth (as recorded in groundmass crystals).

This paper demonstrates the benefit of multi-parametric investigations into volcanic lightning and the broad range of processes that contribute to it.

Acknowledgements

Funding support was made possible by National Science Foundation Grants AGS 1445704 and 1445703, The Jack Kleinman Grant for Volcano Research, and the Fred L. and Helen M. Tharp Fellowship. The manuscript was greatly improved by the reviews of Tamsin Mather, Earle Williams, and one anonymous reviewer.

Appendix A. Supplementary material

Supplementary material related to this article can be found online at https://doi.org/10.1016/j.epsl.2018.03.052.

References

Aizawa, K., Cimarelli, C., Alatorre-Ibargüengoitia, M.A., Yokoo, A., Dingwell, D.B., Iguchi, M., 2016. Physical properties of volcanic lightning: constraints from magnetotelluric and video observations at Sakurajima volcano, Japan. Earth Planet. Sci. Lett. 444, 45–55. https://doi.org/10.1016/j.epsl.2016.03.024.

Aizawa, K., Yokoo, A., Kanda, W., Ogawa, Y., Iguchi, M., 2010. Magnetotelluric pulses generated by volcanic lightning at Sakurajima volcano, Japan. Geophys. Res. Lett. 37, 2–6. https://doi.org/10.1029/2010GL044208.

Aramaki, S., Kobayashi, T., 1986. Change of the whole-rock chemical composition of the recent ejecta of Minamidake, Sakurajima. Bull. Volcanol. Soc. Jpn. 31.

Arason, P., Bennett, A.J., Burgin, L.E., 2011. Charge mechanism of volcanic lightning revealed during the 2010 eruption of Eyjafjallajökull. J. Geophys. Res., Solid Earth 116, 1–15. https://doi.org/10.1029/2011JB008651.

Behnke, S.A., Edens, H.E., Thomas, R.J., Smith, C.M., McNutt, S.R., Van Eaton, A., Cimarelli, C., Cigala, V., 2018. Investigating the origin of continual radio frequency impulses during explosive volcanic eruptions. J. Geophys. Res., Atmos. https://doi.org/10.1002/2017JD027990.

Behnke, S.A., Thomas, R.J., Edens, H.E., Krehbiel, P.R., Rison, W., 2014. The 2010 eruption of Eyjafjallajökull: lightning and plume charge structure. J. Geophys. Res., Atmos. 119, 833–859. https://doi.org/10.1002/2013JD020781.

Behnke, S.A., McNutt, S.R., 2014. Using lightning observations as a volcanic eruption monitoring tool. Bull. Volcanol. 76, 1–12. https://doi.org/10.1007/s00445-014-0847-1.

Behnke, S.A., Thomas, R.J., McNutt, S.R., Schneider, D.J., Krehbiel, P.R., Rison, W., Edens, H.E., 2013. Observations of volcanic lightning during the 2009 eruption of Redoubt Volcano. J. Volcanol. Geotherm. Res. 259, 214–234. https://doi.org/10.1016/j.jvolgeores.2011.12.010.

Behnke, S., Bruning, E., 2015. Changes to the turbulent kinematics of a volcanic plume inferred from lightning data. Geophys. Res. Lett. https://doi.org/10.1002/2015GL064199.

Bennett, A.J., Odams, P., Edwards, D., Arason, Þ., 2010. Monitoring of lightning from the April–May 2010 Eyjafjallajökull volcanic eruption using a very low frequency lightning location network. Environ. Res. Lett. 5, 44013. https://doi.org/10.1088/1748-9326/5/4/044013.

Cashman, K.V., Scheu, B., 2015. Magmatic fragmentation. In: Sigurdsson, H., Houghton, B., McNutt, S.R., Rymer, H., Stix, J. (Eds.), The Encyclopedia of Volcanoes, second ed. Elsevier Inc.

Cimarelli, C., Alatorre-Ibargüengoitia, M.A., Aizawa, K., Yokoo, A., Díaz-Marina, A., Iguchi, M., Dingwell, D.B., 2016. Multiparametric observation of volcanic lightning: Sakurajima Volcano, Japan. Geophys. Res. Lett. 43, 4221–4228. https://doi.org/10.1002/2015GL067445.

Cimarelli, C., Alatorre-Ibargüengoitia, M.A., Kueppers, U., Scheu, B., Dingwell, D.B., 2014. Experimental generation of volcanic lightning. Geology 42, 79–82. https://doi.org/10.1130/G34802.1.

Clarke, A.B., Ongaro, T.E., Belousov, A., 2015. Vulcanian eruptions. In: Sigurdsson, H., Houghton, B., McNutt, S.R., Rymer, H., Stix, J. (Eds.), The Encyclopedia of Volcanoes, second ed. Elsevier Inc.

Dellino, P., Gudmundsson, M.T., Larsen, G., Mele, D., Stevenson, J.A., Thordarson, T., Zimanowski, B., 2012. Ash from the Eyjafjallajokull eruption (Iceland): fragmentation processes and aerodynamic behavior. J. Geophys. Res., Solid Earth 117, 1–10. https://doi.org/10.1029/2011JB008726.

Dufek, J., Manga, M., Patel, A., 2012. Granular disruption during explosive volcanic eruptions. Nat. Geosci. 5, 561–564. https://doi.org/10.1038/ngeo1524.

Durant, A.J., Shaw, R.A., Rose, W.I., Mi, Y., Ernst, G.G.J., 2008. Ice nucleation and overseeding of ice in volcanic clouds. J. Geophys. Res., Atmos. 113, 1–13. https://doi.org/10.1029/2007JD009064.

Folk, R.L., Ward, W.C., 1957. Brazos River bar [Texas]; a study in the significance of grain size parameters. J. Sediment. Res. https://doi.org/10.1306/74D70646-2B21-11D7-8648000102C1865D.

Forward, K.M., Lacks, D.J., Sankaran, R.M., 2009. Charge segregation depends on particle size in triboelectrically charged granular materials. Phys. Rev. Lett. 102, 1–4. https://doi.org/10.1103/PhysRevLett.102.028001.

Hamlin, T.D., 2004. The New Mexico Tech Lightning Mapping Array. New Mexico Institute of Mining and Technology.

Hoblitt, R.P., 1994. An experiment to detect and locate lightning associated with eruptions of Redoubt Volcano. J. Volcanol. Geotherm. Res. 62, 499–517. https://doi.org/10.1016/0377-0273(94)90049-3.

Horwell, C.J., 2007. Grain-size analysis of volcanic ash for the rapid assessment of respiratory health hazard. J. Environ. Monit. 9, 1107–1115. https://doi.org/10.1039/b710583p.

Houghton, I.M.P., Aplin, K.L., Nicoll, K.A., 2013. Triboelectric charging of volcanic ash from the 2011 Grimsvotn eruption. Phys. Rev. Lett. 111, 118501. https://doi.org/10.1103/PhysRevLett.111.118501.

Iguchi, M., Tanegyri, T., Ohta, Y., Ueki, S., Nakao, S., 2013. Characteristics of volcanic activity at Sakurajima Volcano's Showa crater during the period 2006 to 2011. Bull. Volcanol. Soc. Jpn. 58, 115–135. https://doi.org/10.18940/kazan.58.1_115.

James, M.R., Wilson, L., Lane, S.J., Gilbert, J.S., Mather, T.A., Harrison, R.G., Martin, R.S., 2008. Electrical charging of volcanic plumes. Space Sci. Rev. 137, 399–418. https://doi.org/10.1007/s11214-008-9362-z.

James, M.R., Lane, S.J., Gilbert, J.S., 2000. Volcanic plume electrification: experimental investigation of a fracture-charging mechanism. J. Geophys. Res. 105, 641–649. https://doi.org/10.1029/2000JB900068.

Jones, T.J., Russell, J.K., 2017. Ash production by attrition in volcanic conduits and plumes. Sci. Rep. 7, 1–12. https://doi.org/10.1038/s41598-017-05450-6.

Jones, T.J., McNamara, K., Eychenne, J., Rust, A.C., Cashman, K.V., Scheu, B., Edwards, R., 2016. Primary and secondary fragmentation of crystal-bearing intermediate magma. J. Volcanol. Geotherm. Res. 327, 70–83. https://doi.org/10.1016/j.jvolgeores.2016.06.022.

Lacks, D.J., Mohan Sankaran, R., 2011. Contact electrification of insulating materials. J. Phys. D, Appl. Phys. 44, 453001. https://doi.org/10.1088/0022-3727/44/45/453001.

Lane, S.J., Gilbert, J.S., 1992. Electric potential gradient changes during explosive activity at Sakurajima volcano, Japan. Bull. Volcanol. 54, 590–594.

Leibrandt, S., Le Pennec, J.-L., 2015. Towards fast and routine analyses of volcanic ash morphometry for eruption surveillance applications. J. Volcanol. Geotherm. Res. 297, 11–27. https://doi.org/10.1016/j.jvolgeores.2015.03.014.

Lowe, D., 2015. Connecting and dating with tephras: principles, functioning, and application of tephrochronology in Quaternary research. In: 12th Quat. Tech. Short Course – Techniques Palaeoclim. Palaeoenvironmental Reconstr., pp. 1–30.

MacGorman, D.R., Rust, W.D., 1998. The Electrical Nature of Storms. Oxford University Press, New York.

McNutt, S.R., Thomas, R.J., 2015. Volcanic lightning. In: Sigurdsson, H., Houghton, B., McNutt, S.R., Rymer, H., Stix, J. (Eds.), The Encyclopedia of Volcanoes, second ed. Elsevier Inc.

McNutt, S.R., Williams, E.R., 2010. Volcanic lightning: global observations and constraints on source mechanisms. Bull. Volcanol. 72, 1153–1167. https://doi.org/10.1007/s00445-010-0393-4.

Mendez Harper, J., Dufek, J., 2016. The effects of dynamics on the triboelectrification of volcanic ash. J. Geophys. Res., Atmos. 121 (14), 8209–8228. https://doi.org/10.1002/2015JD024275.

Mendez Harper, J., Dufek, J., Mcadams, J., 2015. The electrification of volcanic particles during the brittle fragmentation of the magma column. In: Proc. ESA Annual Meeting on Electrostatics, p. 10.

Miura, T., Koyaguchi, T., Tanaka, Y., 2002. Measurements of electric charge distribution in volcanic plumes at Sakurajima volcano, Japan. Bull. Volcanol. 64, 75–93. https://doi.org/10.1007/s00445-001-0182-1.

Miwa, T., Toramaru, A., Iguchi, M., 2009. Correlations of volcanic ash texture with explosion earthquakes from vulcanian eruptions at Sakurajima volcano, Japan. J. Volcanol. Geotherm. Res. 184, 473–486. https://doi.org/10.1016/j.jvolgeores.2009.05.012.

Okuno, M., Nakamura, T., Moriwaki, H., Kobayashi, T., 1997. AMS radiocarbon dating of the Sakurajima tephra group, Southern Kyushu, Japan. Nucl. Instrum. Methods Phys. Res., Sect. B, Beam Interact. Mater. Atoms 123, 470–474. https://doi.org/10.1016/S0168-583X(96)00614-3.

Rison, W., Thomas, R.J., Krehbiel, P.R., Hamlin, T., Harlin, J., 1999. A GPS-based three-dimensional lightning mapping system: initial observations in central New Mexico. Geophys. Res. Lett. 26, 3573–3576. https://doi.org/10.1016/j.jval.2016.03.1245.

Saunders, C.P.R., Bax-Norman, H., Emersic, C., Avila, E.E., Castellano, N.E., 2006. Laboratory studies of the effect of cloud conditions on graupel/crystal charge transfer in thunderstorm electrification. Q. J. R. Meteorol. Soc. 132, 2653–2673. https://doi.org/10.1256/qj.05.218.

Schill, G.P., Genareau, K., Tolbert, M.A., 2015. Deposition and immersion-mode nucleation of ice by three distinct samples of volcanic ash. Atmos. Chem. Phys. 15, 7523–7536. https://doi.org/10.5194/acp-15-7523-2015.

Schneider, C.A., Rasband, W.S., Eliceiri, K.W., 2012. NIH Image to ImageJ: 25 years of image analysis. Nat. Methods 9 (7), 671–675. PMID 22930834.

Thomas, B.R.J., McNutt, S.R., Krehbiel, P.R., Rison, W., Aulich, G., Harald, E., Tytgat, G., Clark, E., 2010. Lightning and electrical activity during the 2006 eruption of Augustine Volcano. In: Power, J.A., Coombs, M.L.A., Freymueller, J.T. (Eds.), The 2006 Eruption of Augustine Volcano. In: U.S. Geological Survey Professional Paper, Alaska, pp. 579–608.

Thomas, R., Krehbiel, P., Rison, W., Harlin, J., Hamlin, T., Campbell, N., 2003. The LMA flash algorithm. In: Proc. 12th Int. Conf. on Atmospheric Electricity, International Commission on Atmospheric Electricity Versailles, France, pp. 655–656.

Thomas, R.J., Krehbiel, P.R., Rison, W., Edens, H.E., Aulich, G.D., Winn, W.P., McNutt, S.R., Tytgat, G., Clark, E., 2007. Electrical activity during the 2006 Mount St. Augustine volcanic eruptions. Science 315 (5815), 1097.

Thomas, R.J., Krehbiel, P.R., Rison, W., Hunyady, S.J., Winn, W.P., Hamlin, T., Harlin, J., 2004. Accuracy of the lightning mapping array. J. Geophys. Res. D, Atmos. 109, 1–34. https://doi.org/10.1029/2004JD004549.

Toramaru, A., Noguchi, S., Oyoshihara, S., Tsune, A., 2008. MND (microlite number density) water exsolution rate meter. J. Volcanol. Geotherm. Res. 175, 156–167. https://doi.org/10.1016/j.jvolgeores.2008.03.035.

Van Eaton, A.R., Amigo, A., Bertin, D., Mastin, L.G., Giacosa, R.E., Gonzalez, J., Valderrama, O., Fontijn, K., Behnke, S.A., 2016. Volcanic lightning and plume behavior reveal evolving hazards during the April 2015 eruption of Calbuco volcano, Chile. Geophys. Res. Lett. 43 (7), 3563–3571. https://doi.org/10.1002/2016GL068076.

Van Eaton, A.R., Mastin, L.G., Herzog, M., Schwaiger, H.F., Schneider, D.J., Wallace, K.L., Clarke, A.B., 2015. Hail formation triggers rapid ash aggregation in volcanic plumes. Nat. Commun. 6, 1–7. https://doi.org/10.1038/ncomms8860.

Williams, E.R., McNutt, S.R., 2005. Total water contents in volcanic eruption clouds and implications for electrification and lightning. In: Recent Prog. Light. Physics, pp. 81–93.

Williams, E., Nathou, N., Hicks, E., Pontikis, C., Russell, B., Miller, M., Bartholomew, M.J., 2009. The electrification of dust-lofting gust fronts ('haboobs') in the Sahel. Atmos. Res. 91, 292–298. https://doi.org/10.1016/j.atmosres.2008.05.017.